Science Advances
AAAS

Supplementary Materials for

Emergent second-harmonic generation in van der Waals heterostructure of bilayer MoS_2 and monolayer graphene

Mingwen Zhang *et al.*

Corresponding author: Xuetao Gan, xuetaogan@nwpu.edu.cn

Sci. Adv. **9**, eadf4571 (2023)
DOI: 10.1126/sciadv.adf4571

This PDF file includes:

Supplementary Text

Section S1. Interfacial quality of the 2LM/1LG

Thermal annealing is commonly used to remove residues and improve the interfacial quality of vdWHs (*31*, *18*). Here, the heterointerfaces of the 2LM/1LG vdWH are characterized by the atomic force microscope (AFM). Figure S1A shows the AFM image of the as-transferred 2LM/1LG vdWH and the height of the 2LM flake on the 1LG flake is measured as 4 nm. This value is much larger than the expected 1.3 nm thickness of 2LM (*38*), which may result from the molecules absorbed between the layers since the transfer process is performed in the air. The white dots on the surface of 2LM/1LG in the AFM image are bubbles, indicating the existence of trapped gas molecules between the 2LM and 1LG layers. The schematic illustration of the air gap is shown in Fig. S1B. After vacuum annealing at 300 °C for 30 min, as depicted in Fig. S1C, the height of the 2LM flake on the 1LG is decreased to 1.3 nm, which is almost identical to the thickness of pristine 2LM.

The annealing treatment releases the stress and drives away the air gap between 2LM and 1LG, which twists part of the 2LM layer and leaves a wrinkle, as well as two flat regions with high interface quality which are labeled as A and B in Fig. 3A. Both regions A and B have high-quality interfaces, which can be seen from the AFM image in Fig. S1C, as both are flat and smooth. The twist angle between A and B can be determined from the original straight boundary of 2LM (the white solid line in Fig. S1C) and the boundary of the twisted 2LM (the white dotted line in Fig. S1C), which is about 15°.

Section S2. Raman spectroscopy for determining the interlayer coupling in 2LM/1LG

Figure S2 shows the acquired Raman spectrum at the shear (S) mode and layer-breathing (LB) mode range acquired from the 2LM/1LG region before and after the annealing. The S and LB modes have been proven to be sensitive to the interlayer coupling of 2DMs and also the interfacial coupling of two-dimensional heterostructures (*18*, *52*). The peak position of LB mode shifts from 40 cm^{-1} in pristine 2LM to 35 cm^{-1} in 2LM/1LG, which indicates the interface LB force constant of the 2LM/1LG as 60×10^{18} N/m^3 using the linear chain model (*18*). This value is comparable with that of multilayer MoS_2 and graphene flakes, confirming the emergence of the strong interlayer coupling in 2LM/1LG. Strong interlayer coupling and SHG are observed simultaneously in annealed 2LM/1LG, indicating that there is a correlation between interlayer coupling and SHG.

Section S3. Determination of the thickness of MoS_2 and graphene

The 2LM and 1LG flakes are first distinguished by optical microscope using the optical contrast method. Then we use Raman spectroscopy to determine the specific layer numbers of the samples. All Raman spectra are recorded at room temperature in the air using the confocal WiTec Alpha 300R Raman Microscope. The wavelength of the excitation laser is 532 nm. The excitation power is 1 mW (for 1LG) and 0.2 mW (for 2LM) to avoid the laser heating effect. As shown in Fig. S3A, the shear (S) mode at 23 cm^{-1} and layer breathing (LB) mode at 40 cm^{-1} of ultra-low frequency Raman spectrum indicate that the MoS_2 sample is a bilayer (*52*). Figure S3B shows the Raman spectra of 1LG where the G' band can be fitted by just one Lorentzian with a full width at half

maximum of 24 cm^{-1}. No D band is observed at ~1350 cm^{-1}, which indicates the high quality of 1LG (*53*).

Section S4. Multiphoton Nonlinear Optical Microscopy System

SHG measurements of the BLG are implemented in a home-built multiple-photon spectroscopy system with the reflection geometry, as illustrated in Fig. S4. The fundamental pump from a picosecond pulsed laser at the wavelength of 1064 nm is linearly polarized via a polarizer. Then it is reflected by a dichroic mirror and focused on the sample through a 100× objective lens with a numerical aperture (NA) of 0.8. The generated SHG radiation is then back collected by the same objective and passes through the dichroic mirror, which is subsequently coupled to a spectrometer mounted with a cooled silicon CCD camera for spectra measurements.

For SHG spatial mapping, samples are placed on a piezo-actuated stage with a minimum moving step of 500 nm for the in-plane scanning, while the excitation and collection light spots are fixed. To study the polarization dependence of the SHG radiation, another polarizer is placed in the signal collection path, whose direction is rotated correspondingly to the pump polarization to collect the parallel or perpendicular components of the SHG signal. We note here that the polarizer is not placed in the signal path for spectra measurements.

Section S5. SHG at different stages during the vdWH fabrication

No SHG but only the broadband NPL from the underlying 1LG in the 2LM/1LG region just after the transfer of 2LM, as shown in the green curve in Fig. S5. After the vacuum annealing at 300℃, the SHG emerges in 2LM/1LG, as shown in the blue curve.

Section S6. Raman spectra of 2LM at different stages during the vdWH fabrication

The Shear (S) and Layer-breathing (LB) modes remain unchanged in pristine 2LM, annealed 2LM, and as transferred 2LM/1LG. The position of E_{2g}^1 mode remains unchanged in annealed 2LM, while it redshifts in as transferred 2LM/1LG. It shifts back to the same position as that of pristine 2LM. For A_{1g} mode, it remains unchanged in pristine 2LM, annealed 2LM, and as transferred 2LM/1LG. It blue shifts in annealed 2LM/1LG.

Considering that the E_{2g}^1 and A_{1g} modes of 2LM are sensitive to strain and charge doping respectively, we can get the change of strain and charge doping in 2LM through the shifts of these two Raman modes. The red shift of the E_{2g}^1 mode in as transferred 2LM indicates that the 2LM is under strain, while it shifts back to the same position as 2LM after the annealing treatment, which means that the annealing process releases the stress or strain in 2LM. For A_{1g} mode, the blue shift in the annealed 2LM/1LG may indicate the charge dope and the interlayer coupling between 2LM and 1LG. The invariance of the A_{1g} mode position in the other three cases shows that charge transfer and interlayer coupling do not exist.

Section S7. Exclusion of the strain effect in 2LM/1LG.

For graphene, as reported in (*39*), G' peak would split into two peaks, and they altogether redshift. In our experiment, we compare the G' peak in graphene at different stages of the vdWH fabrication, there is no observable splitting and redshift. From different samples (in Fig. 2 and Fig. 5), only the blueshifts of the G' peak are observed. We could therefore exclude the strain in graphene of the vdWH of 2LM/1LG.

For MoS_2, as reported in (*38*), the in-plane E_{2g}^1 Raman mode is sensitive to strain and the A_{1g} mode has no obvious shift to strain. In our 2LM/1LG sample, as shown in the Raman spectra shown in Fig. S6, there is a redshift of the E_{2g}^1 mode in 2LM after its transfer on the 1LG, indicating the existence of strain in the as-transferred 2LM/1LG. However, after annealing treatment, the 2LM/1LG realizes the actual vdW stacking and the E_{2g}^1 mode shifts back to the same position as the separate 2LM. It means that the annealing process releases the strain in 2LM. Hence, we could exclude the strain in the 2LM of the 2LM/1LG.

Section S8. Gate-tunable SHG in 2LM/1LG

We fabricate another vdWH device of 2LM/1LG with metal electrodes (see the insets of Fig. S8A). Since the vdWH is fabricated on a highly doped silicon substrate with a thin SiO_2 dielectric layer, the Fermi levels could be tuned by applying a back gate voltage (V_g). With the application of varied V_g, the SHG signal from the vdWH region varies (see Fig. S8A). When the positive V_g is applied and increased, the SHG signal decreases gradually. Here, to avoid the breakdown of the SiO_2 layer, the V_g is limited to 60 V (-60 V). At 60 V, the SHG intensity is decreased to half of the value without gating. It is expected that zero SHG could be achieved if the V_g were increased further. If the V_g is applied along the opposite direction, the SHG signal is increased gradually when the V_g value is increased.

To explain this electrically tuned SHG, we measure the corresponding V_g-dependent Raman spectra. Figure S8B and Fig. S8C show the featured Raman spectra of the 1LG and 2LM of the 2LM/1LG heterostructure under different V_g. The G, G', and A_{1g} modes show no obvious shift with the variation of V_g, which indicates that the charge transfer between 2LM and 1LG is not modulated by the V_g. That is, the ground state charge transfer between 2LM and 1LG has been determined when the heterostructure is formed. The S and LB modes of 2LM in 2LM/1LG also remain unchanged with the variation of V_g. However, the applied V_g can change the charge distribution in the heterostructure and affect the symmetry, based on our first principles calculations. Figure S8D and Fig. S8E show the calculated charge density difference of the 2LM/1LG heterostructure under different V_g. When the V_g is applied, the external electric field (E_{field}) caused by the V_g drives the charge to redistribute in the 2LM. As shown in Fig. S8D, compared with the situation when V_g = 0 V (Fig. 2C), the electrons accumulate at the top of the MoS_2 bilayer with E_{field} = 0.01 V/Å. In another case, when V_g is applied along the negative direction, the electrons deplete at the top of the MoS_2 bilayer with E_{field} = -0.01 V/Å, as shown in Fig. S8E.

Section S9. Polarization-resolved SHG in 2LM/1LG, 4LM/1LG, and 6LM/1LG vdWHs

The even-number-layered MoS_2 is first prepared on the PDMS substrate, and the boundaries of 2LM and 4LM are originally parallel before transferring on 1LG. Due to the existence of strain in

the process of dry transfer, the 2LM part is torn apart and separated from the 4LM, forming a twist angle between 2LM and 4LM. From the two dashed lines in Fig. S9A (the green dashed line for the boundary of 4LM and the orange one for 2LM, respectively), the twist angle is determined to be about 2°. The polarization dependences of the SHGs from the regions of 2LM/1LG, 4LM/1LG, and 6LM/1LG vdWHs are shown in Fig. S9B. The two dashed lines in Fig. S9B indicate the orientation of the polarization-resolved SHG patterns from 2LM/1LG and 4LM/1LG, which shows a twisted angle of 2° by fitting. However, the polarization-resolved SHG patterns of 4LM/1LG and 6LM/1LG show no twist angle, which is consistent with the device structure. The variation of SHG intensities in different vdWH regions here is also consistent with the result in Fig. 5 in the main text.

Section S10. Charge transfers and density distributions in 2LM/1LG and 4LM/1LG

The first-principles calculations were employed to calculate charge density distributions in the 2LM/1LG and 4LM/1LG vdWHs, which could clearly reveal the charge transfer and symmetry breaking in the vdWHs, as shown in Fig. S10. The calculated results were displayed with different isosurface levels of net charges, where Figs. S10A-C are the cases with levels chosen as 1×10^{-4} e/Å^3, 5×10^{-5} e/Å^3 and 3×10^{-5} e/Å^3, respectively. When the charge isosurface level is chosen with a high level of 1×10^{-4} e/Å^3 (see Fig. S10A), in both 2LM/1LG and 4LM/1LG, most of the electrons transferred from the 1LG are concentrated on the lower sulfur (S) atom of the bottom (1st) MoS_2 layer, and the charge distribution of the upper MoS_2 layers is almost not affected. By reducing the charge isosurface levels to 5×10^{-5} e/Å^3 (see Fig. S10B) and 3×10^{-5} e/Å^3 (see Fig. S10C). There are non-uniform charge distributions over the upper (2nd, 3rd, 4th) MoS_2 layers in the 4LM/1LG vdWH. On the 2nd and 3rd MoS_2 layers, there is no charge transferred in or out, and only the shift of the positive and negative charges with respect to the plane of the molybdenum (Mo) atom layer. On the 4th MoS_2 layer, there are electrons transferred around it. In summary, after the vdW contact of 4LM and 1LG, the charge transfer mainly occurs at the interface of the bottom MoS_2 layer and 1LG, and electrons mainly concentrate on the bottom S atom. Comparatively, the charge transfer inside the 4LM is much weaker, though the uppermost MoS_2 layer acquires few electrons. As a consequence, over the 4LM, the charge distribution is strongly unbalanced, which results in the inversion symmetry breaking for yielding the effective second-order hyperpolarizability and SHG.

Section S11. Absorption characteristics of even-number-layered MoS_2

We perform differential reflection measurements to characterize the absorption properties of even-number-layered MoS_2. The results are shown in Fig. S11. Here the differential reflection is defined as $\Delta R/R_0=(R-R_0)/R_0$, where R and R_0 are the reflectances of the MoS_2 sample and the transparent PDMS substrate, respectively. As shown in the spectra, the absorption of MoS_2 at the wavelength of 532 nm increases with the increase of the number of layers, which is consistent with the conclusion that the re-absorption of SHG photons by MoS_2 with different layer numbers plays the dominating role in the variation of the SHG intensities in their heterostructures with monolayer graphene (see Fig. 5 in the main text).

Section S12. Emergent SHG in van der Waals heterostructure of bilayer WSe_2 and monolayer graphene

We first mechanically exfoliated 1LG on a SiO_2/Si substrate using the standard scotch tape method. The bilayer WSe_2 (2LW) flake was exfoliated on a PDMS stamp, which was then transferred onto the prepared 1LG by the all-dry transfer method. A vacuum annealing process at 300°C was carried out for 30 minutes. The optical microscope image of the fabricated 2LW/1LG is shown in Fig. S12A. Figure S12B shows the acquired frequency up-converted optical spectra from 2LW and 2LW/1LG. From the region of 2LW/1LG, a sharp peak appears at 532 nm, which is exactly half of the pump wavelength. It indicates the emergence of SHG. In contrast, there is no SHG signal in the separate 2LM region. The spatial mapping result of the signal at the wavelength of 532 nm is displayed in Fig. S12C, showing a clear and continuous region with an obvious SHG signal from the 2LW/1LG. The dependence of SHG intensity on the pump power is measured from the 2LW/1LG, as shown in Fig. S12D, which shows a slope of 2.23 in the log-log plot and confirms its second-order nonlinear process.

Section S13. Emergent SHG in van der Waals heterostructure of monolayer ReS_2 and bilayer MoS_2.

The bilayer MoS_2 (2LM) and monolayer ReS_2 (1LR) are mechanically exfoliated on PDMS. Then the 2LM is transferred onto the SiO_2/Si substrate using the all-dry transfer method. After that, the 1LR is stacked on the 2LM using the same method to form the vdWH. A vacuum annealing process at 300°C is carried out for 30 minutes. Figure S13A shows the optical microscope image of the fabricated vdWH. Figure S13B shows the acquired SHG spectra from the separate 2LM and 1LR/2LM, where we can see a sharp SHG signal in the 1LR/2LM which is absent in the separate 2LM. We note here that the wavelength of the incident light is 1550 nm, so the SHG signal appears at exactly 775 nm. The spatial mapping of this SHG is shown in Fig. S13C where the SHGs distribute in the 1LR/2LM region. The slope of 1.97 in the log-log plot of the power-dependent SHG intensity is shown in Fig. S13D, which is consistent with the SHG process where the two incident photons convert into one photon.

Fig. S1

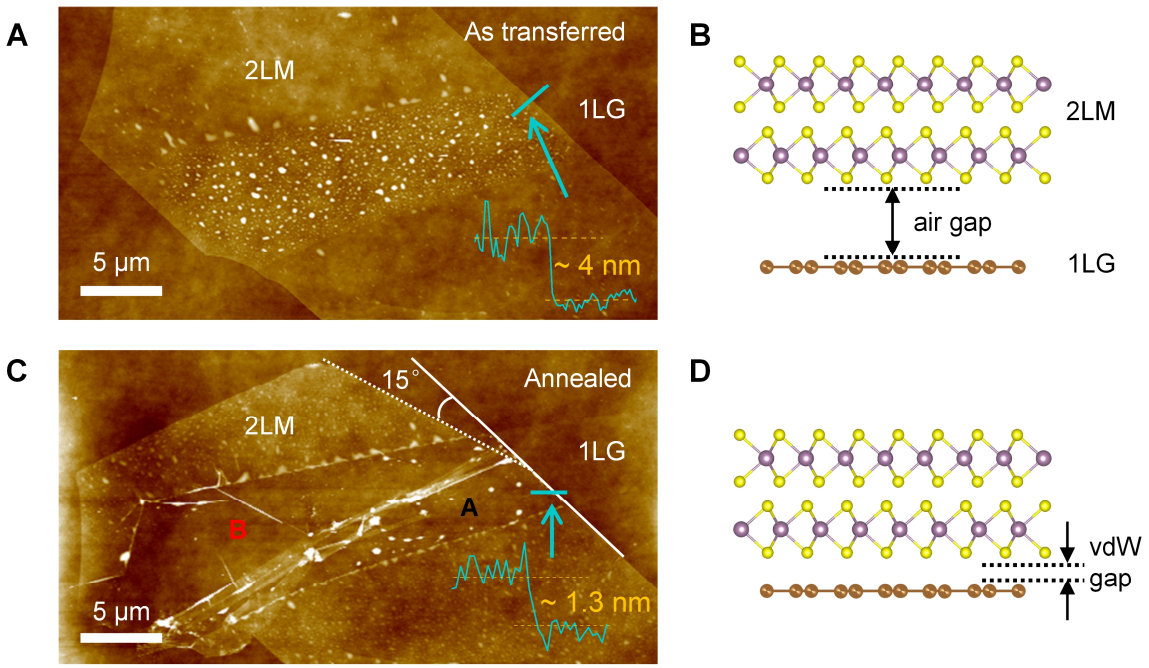

Fig. S1.

Interfacial quality of the 2LM/1LG. AFM images of (**A**) as-transferred and (**C**) annealed 2LM/1LG, in which the height profile of the 2LM on the 1LG is shown for each image. Schematic illustration of the interlayer gap of (**B**) as-transferred and (**D**) annealed 2LM/1LG.

Fig. S2

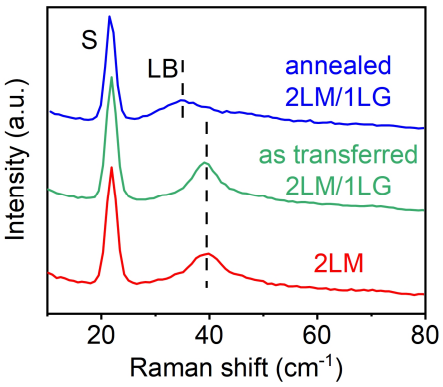

Fig. S2.

Low-frequency Raman spectra of the separate 2LM and 2LM/1LG. Here, S and LB mark shear and layer-breathing modes, respectively.

Fig. S3

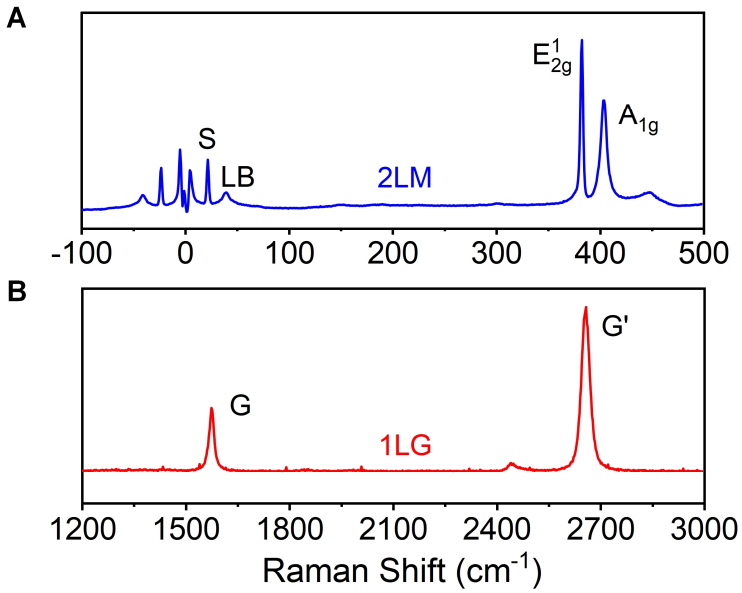

Fig. S3.

Raman spectroscopy of 2LM and 1LG. (A) Raman spectrum of 2LM. The S and LB refer to the shear mode and layer-breathing mode, respectively. (B) Raman spectrum of 1LG.

Fig. S4

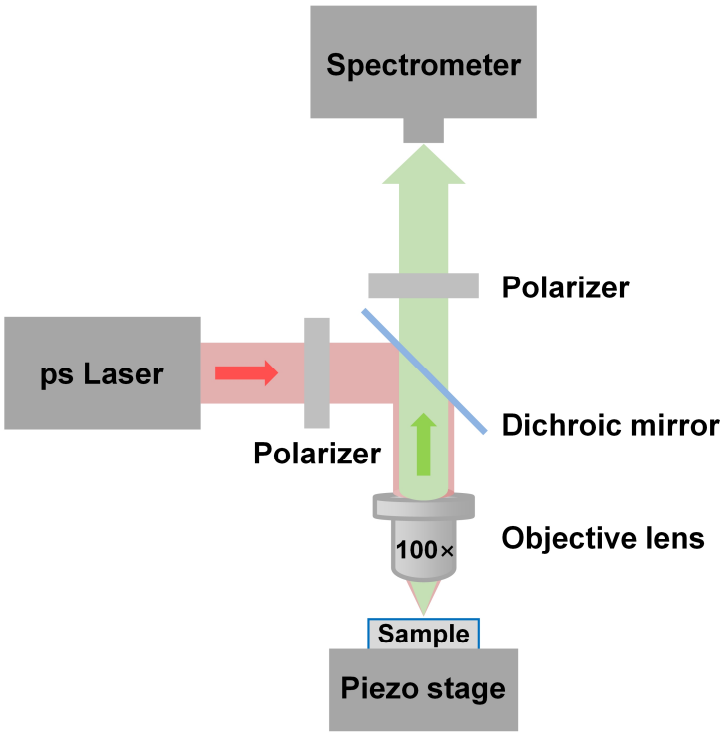

Fig. S4.
Schematic illustration of multiphoton nonlinear optical spectroscopy system.

Fig. S5

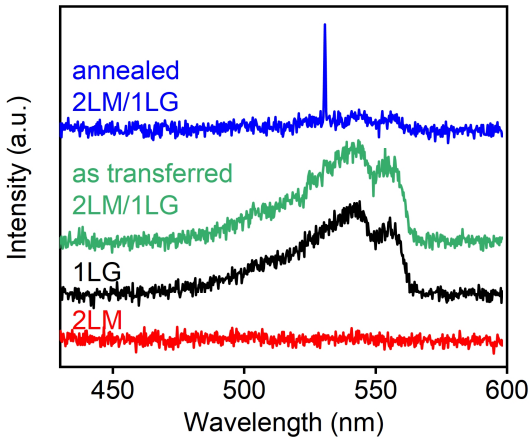

Fig. S5.

Frequency up-converted optical spectra of pristine 2LM, pristine 1LG, as transferred 2LM/1LG and annealed 2LM/1LG.

Fig. S6.

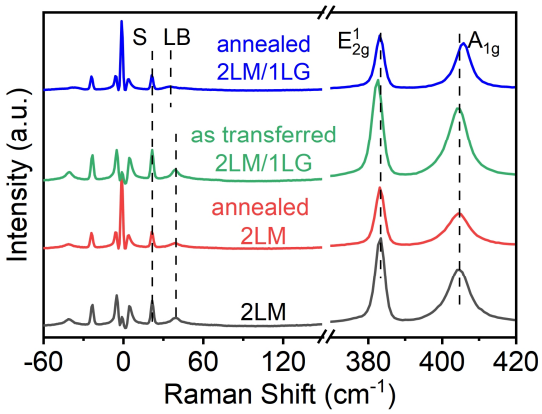

Fig. S6

Raman spectra of 2LM at different stages during the vdWH fabrication.

Fig. S7

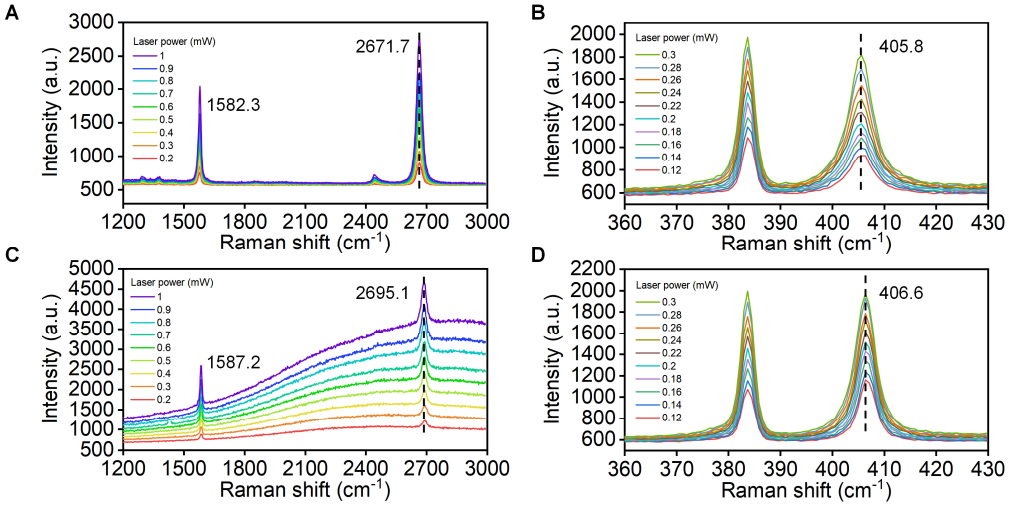

Fig. S7

Power dependence of Raman spectra. (A, B) Power-dependent Raman spectra in the separated 1LG **(A)** and 2LM **(B)**. **(C, D)** Power-dependent Raman spectra of 1LG **(C)** and 2LM **(D)** in the 2LM/1LG vdWH.

Fig. S8

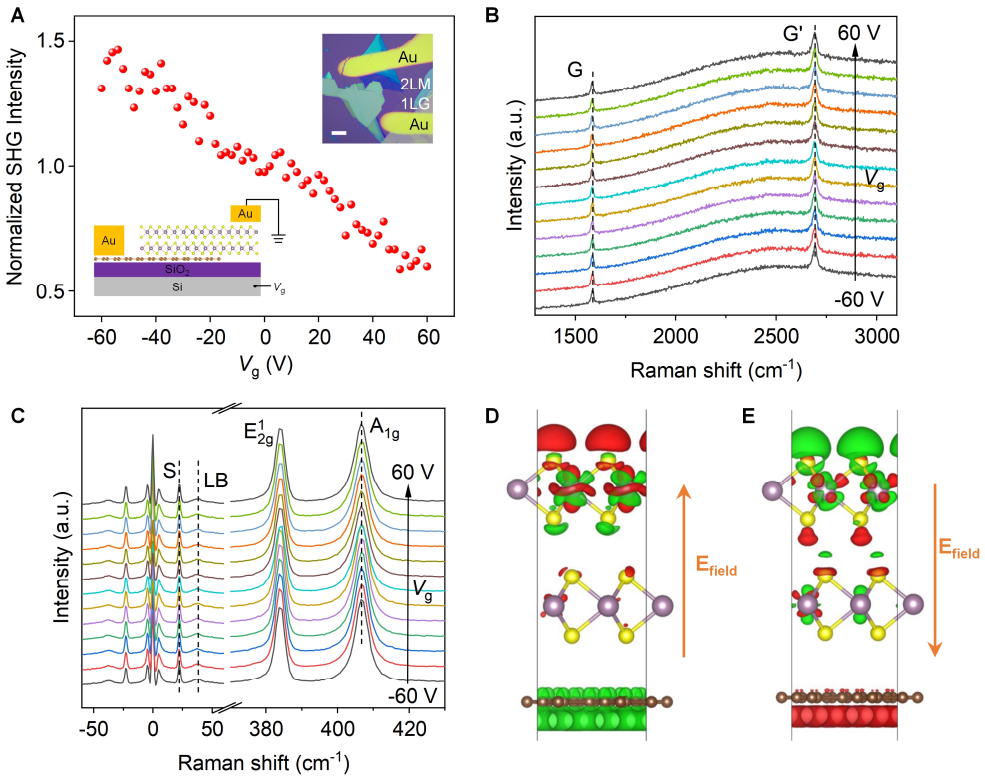

Fig. S8

Gate-tunable SHG in 2LM/1LG. (A) V_g-dependent SHG intensity in 2LM/1LG. Bottom inset: schematic illustration of the device. Top inset: optical microscope image of the device. (**B, C**) V_g-dependent Raman spectra of 1LG and 2LM in 2LM/1LG. **(D, E)** Charge density difference of 2LM/1LG between the case without E_{field} and the case with E_{field} = 0.01 V/Å (**D**) and E_{field} = -0.01 V/Å (**E**). The isosurface here is taken to be 4×10^{-6} e/Å^3. The red and green regions represent the accumulation and depletion of electrons, respectively.

Fig. S9

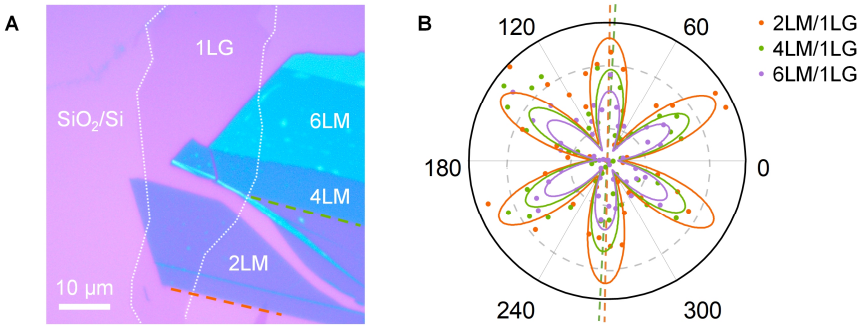

Fig. S9

Polarization-resolved SHG in 2LM/1LG, 4LM/1LG, and 6LM/1LG vdWHs. (**A**) Optical microscope images of 2LM/1LG, 4LM/1LG, and 6LM/1LG vdWHs. (**B**) Polarization-resolved SHG patterns of the 2LM/1LG, 4LM/1LG, and 6LM/1LG .

Fig. S10

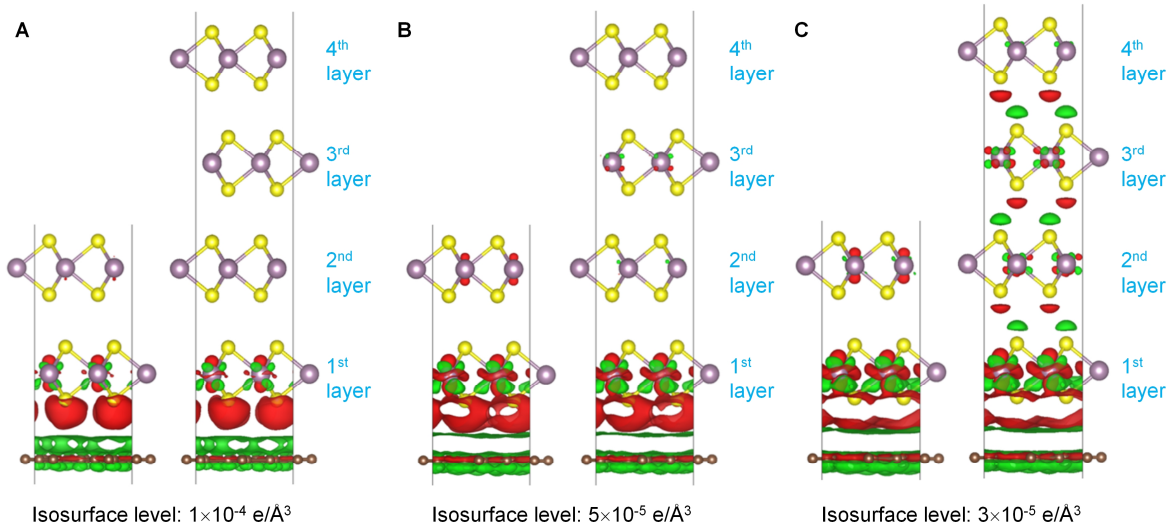

Fig. S10

Charge transfers and density distributions in 2LM/1LG and 4LM/1LG. Side view of isosurface plots of the induced charge density differences after 2LM (4LM) and 1LG form the vdWH. The isosurfaces are taken with levels of (A) 1×10^{-4} e/Å^3, (B) 5×10^{-5} e/Å^3 and (C) 3×10^{-5} e/Å^3. The red and green regions represent the accumulation and depletion of electrons, respectively.

Fig. S11

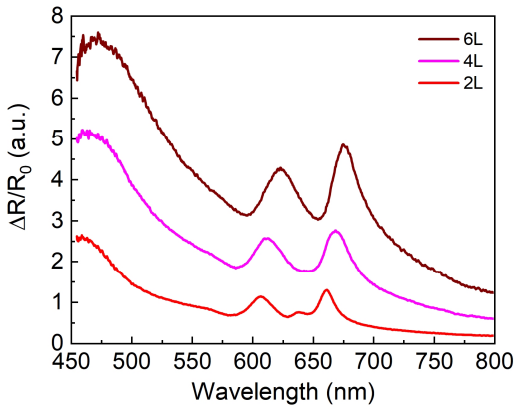

Fig. S11

Differential reflection spectra of even-number-layered MoS_2.

Fig. S12

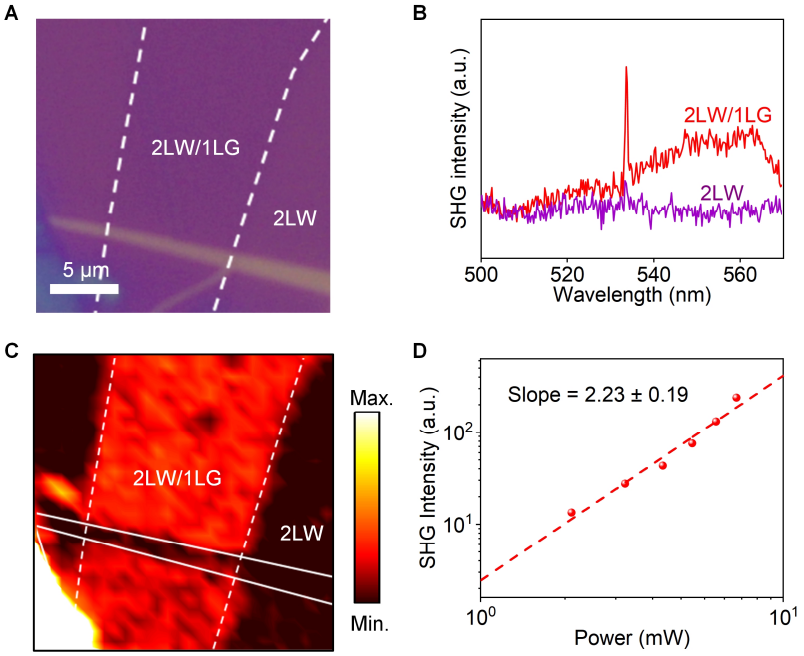

Fig. S12

Emergent SHG in van der Waals heterostructure of bilayer WSe_2 and monolayer graphene. (**A**) Optical microscope image of 2LW/1LG vdWH formed by transferring 2LW on 1LG. The 1LG is marked by the white dashed line. (**B**) Frequency up-converted optical spectra measured from different regions shown in (**A**). (**C**) Spatial SHG mapping of the sample in (**A**) at the wavelength of 532 nm. (**D**) Log-log plot of pump power dependence of the SHG intensity in 2LW/1LG.

Fig. S13

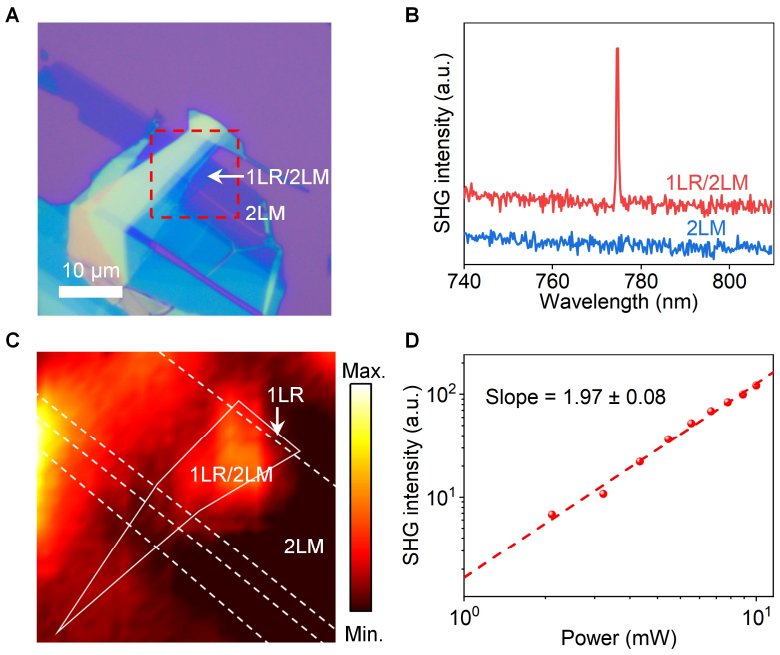

Fig. S13

Emergent SHG in van der Waals heterostructure of monolayer ReS_2 and bilayer MoS_2. (**A**) Optical microscope image of 1LR/2LM vdWH. (**B**) Frequency up-converted spectra measured from different regions shown in (**A**). (**C**) Spatial mapping of the SHG in the red dashed line in (**A**). (**D**) Log-log plot of pump power dependence of the SHG intensity in 1LR/2LM.